applied sciences

MDPI

Article

Modeling and Analysis of a Long-Range Target Localization Problem Based on an XS Anode Single-Photon Detector

Yihang Zhai [1,2], Bin Wang [1,3,*], Xiaofei Wang [3,*] and Qiliang Ni [1]

[1] Changchun Institute of Optics, Fine Mechanics and Physics, Chinese Academy of Sciences, Changchun 130033, China; zhaiyihang21@mails.ucas.ac.cn (Y.Z.); niqiliang@hotmail.com (Q.N.)
[2] University of Chinese Academy of Sciences, Beijing 100049, China
[3] Key Laboratory for Applied Statistics of MOE, School of Mathematics and Statistics, Northeast Normal University, Changchun 130024, China
* Correspondence: eatingbeen@hotmail.com (B.W.); wangxf341@nenu.edu.cn (X.W.)

Featured Application: Our research can be used in the direction of space target cataloging, orbit prediction and astronomical observation.

Abstract: With the development of space detection technology, the detection of long-range dark and weak space targets has become an important issue in space detection. Cross-strip anode photon imaging detectors can detect weak light signals with extremely low dark count rates and are well suited to applications in long-range target detection systems. Since cross-strip anode detectors are expensive to develop and fabricate, a theoretical analysis of the detection process is necessary before fabrication. During the detection process, due to the dead time of the detector, some photon-generated signals are aliased, and the true arrival position of the photon cannot be obtained. These aliased signals are usually removed directly in the conventional research. But in this work, we find that these aliased signals are not meaningless and can be applied to center of mass detection. Specifically, we model the probabilistic mechanisms of the detection data, compute the average photon positions using aliased and non-aliased data and prove that our method provides a lower variance compared to the conventional method, which only uses non-aliased data. Simulation experiments are designed to further verify the effectiveness of the aliasing data for detecting the center of mass. The simulation results support that our method of utilizing the aliasing data provides more accurate detection results than that of removing the aliasing data.

Keywords: cross strip anode; single-photon detection; center of mass detection

Citation: Zhai, Y.; Wang, B.; Wang, X.; Ni, Q. Modeling and Analysis of a Long-Range Target Localization Problem Based on an XS Anode Single-Photon Detector. *Appl. Sci.* **2024**, *14*, 2400. https://doi.org/10.3390/app14062400

Academic Editors: Uma Maheswari Rajagopalan and Yoshikazu Koike

Received: 2 January 2024
Revised: 10 March 2024
Accepted: 11 March 2024
Published: 12 March 2024

1. Introduction

Since photon-counting imaging detectors can detect weak signals, they can be applied to quantum communication, sensing and metrology [1]. Moreover, photon-counting imaging detectors can be used to measure the electric field of terahertz radiation [2], detect the composition of dark matter [3] and carry out low-light-level time-resolved fluorescence microscopy [4–9]. In order to improve the efficiency and quality of the detection, researchers are constantly improving and refining the detectors [10].

In photon-counting imaging detectors, the dark count rate and readout noise are very important factors that affect the detection accuracy. A very low dark count rate and very low readout noise means that the detector can record the echo signal very accurately, even if the echo signal is very weak. A cross-strip (XS) anode detector based on a microchannel plate (MCP) and a position-sensitive anode has a very low dark count rate and very low readout noise. The XS anode detector was first proposed and successfully developed by Siegmund et al. at the University of California, Berkeley, in 1998 [11]. The anode design, imaging simulations and imaging algorithms for XS anodes continued to be investigated over the next 20 years or so [12–16]. To the best of our knowledge, an XS detector can

achieve a high spatial resolution of 5–25 μm and a high count rate of 10^7 counts/s, and an XS detector has a long lifetime. XS anode detectors, with their excellent properties, are used in long-range space exploration systems such as the World Space Observatory-Ultraviolet (WSO-UV) [17] and the Colorado High-Resolution Echelle Stellar Spectrograph (CHESS) [18].

The XS anode is a charge-splitting anode consisting of multiple layers of strip electrodes and ceramic insulation. The XS anode receives the electron cloud emitted by the MCP stack using independent microstrips as the charge-splitting electrodes, each connected to an identical and independent circuit detector [19]. As shown in Figure 1, a photon is incident on a photocathode through a window. The photocathode converts it into a photoelectron, which is multiplied by the MCP stack into an electron cloud containing about 10^7 electrons. The electron cloud from the MCP stack falls onto the XS anode, and the charge of the cloud is collected by the electrodes of the anode. Furthermore, the charge pulse signals are amplified using a front-end charge amplifier circuit and then digitized using a digital acquisition circuit and transmitted to a host computer. Finally, position decoding of the incident event is required to obtain the position coordinates of the photons arriving at the detector. Various algorithms can be used for position decoding [20–22], such as the Gaussian three-point center of mass algorithm, center of gravity algorithm, Lorentzian algorithm, Parabola algorithm, Hyperbolic cosine algorithm, weighted center of gravity algorithm, ratio method, generalized ratio method, generalized method and so on.

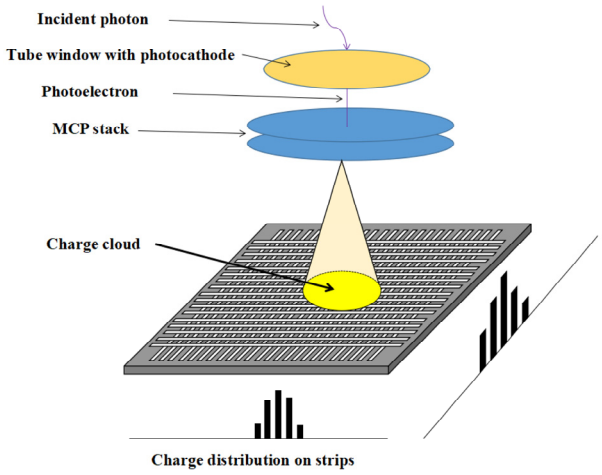

Figure 1. Schematic diagram of XS detector structure.

In conventional XS detection, the detector receives the photons emitted by the target and accumulates the number of photons per pixel to produce an image. When an XS is used for target localization, more attention is often paid to the location of the center of mass of the detected target. In the imaging process, an object point does not correspond to a sharp point on the image plane but diffuses into a spot. Even a small object can diffuse into a larger spot on the detector's image plane, making it difficult to distinguish the exact location of the object. This detection method requires that the time interval between two photons arriving at the detector in close spatial proximity be greater than the dead time. Otherwise, the signals generated by the two photons will be superimposed during Gaussian shaping. The aliased signals result in the detector not being able to correctly obtain the position of the photons. These aliased data are generally regarded as noise and are rejected in conventional XS detection.

Using conventional detection methods, the percentage of aliased data increases as the number of photons emitted by the target increases. This leads to more data being removed and can seriously reduce the efficiency of detecting the target's center of mass. For a given requirement for detecting errors, longer detection times are required. The conventional methods make it difficult to localize targets that emit too many photons because the aliasing data make up the majority of the overall data. Attempts need to be made to attenuate or

limit the photon count. However, even in the case of small photon counts, aliasing the data may occur.

To handle aliased data for a Charge-Coupled Device (CCD) detector, there exist feasible ways [23,24] to separate the aliased signals into several independent ones. But for an XS detector, it is hard for us to accurately separate the aliased data, especially considering the complex correspondence between the X and Y coordinates. Specifically, the XS anode consists of some anode strips in the X direction and some anode strips in the Y direction. When an electron cloud generated by a photon falls onto the XS anode plane, we can only obtain the charge of each anode strip. As shown in Figure 1, one anode strip can only obtain one set of charge data. We need to use these data to calculate the center of mass position of the photon. The processes of calculating the center of mass in the X direction and the center of mass in the Y direction using these data are completely independent. When there is only one photon in a single acquisition result, the X coordinate and Y coordinate of the center of mass can correspond. When two or more photons are included in a single acquisition result, as shown in Figure 2a,b, even if the center of mass can be calculated, it is very hard to realize the correspondence between the X and Y coordinates, and thus the actual positions of the photons cannot be obtained.

In the detection process using an XS detector, each acquisition does not produce an image. Our goal is to employ the detector for target localization instead. For the center of mass detection problem and the target localization problem, neither the exact separation of the aliased data nor of the one-to-one X and Y coordinates is necessary. In this paper, we attempt to directly utilize aliased data to solve center of mass detection and target localization problems. For aliasing the data generated by the superposition of multiple photon signals, this paper analyzes their generation and data composition and finds that these aliasing data can be used for center of mass detection. In this paper, simulation experiments are designed to verify the effectiveness of aliasing data for center of mass detection. This means that in center of mass detection, the effect of the dead time on the detection results will be greatly reduced, and the number of photons need not be limited. In the simulation experiments, the results of retaining the aliased data for center of mass calculations are more accurate than the method of removing the aliased data for the same detection time. In long-range target localization problems based on cross-strip anode detectors, the retention method can obtain the target center of mass more efficiently and accurately. The retention method reduces the time required for detection and can be applied to objects with different brightness levels.

Our research can provide some guidelines and support for the design and fabrication of XS detectors. We can add a new mode of operation to the detector. When the detector is working on target localization, we need the detector to acquire and output both aliased and non-aliased data. When the detector is used for other tasks, it only needs to output non-aliased data. Besides the design of new XS detectors, our work also has potential applications in the future to star sensors and detection in the Earth's shadow. A target in the Earth's shadow is usually dark because it cannot reflect sunlight. We can use a laser to illuminate the target for localization. Compared to conventional CCD-based detectors, XS detectors have the capability for a single-photon response, low readout noise and a very low dark count rate. As shown in this work, by using our proposed center of mass algorithm, an XS detector without a high-power laser requirement could provide accurate localization for dark targets. Star sensors with XS detectors can obtain a space vehicle's attitude by detecting the center of mass of stars at different positions. By applying our algorithm to star sensors, we can achieve efficient detection of the space vehicle's attitude.

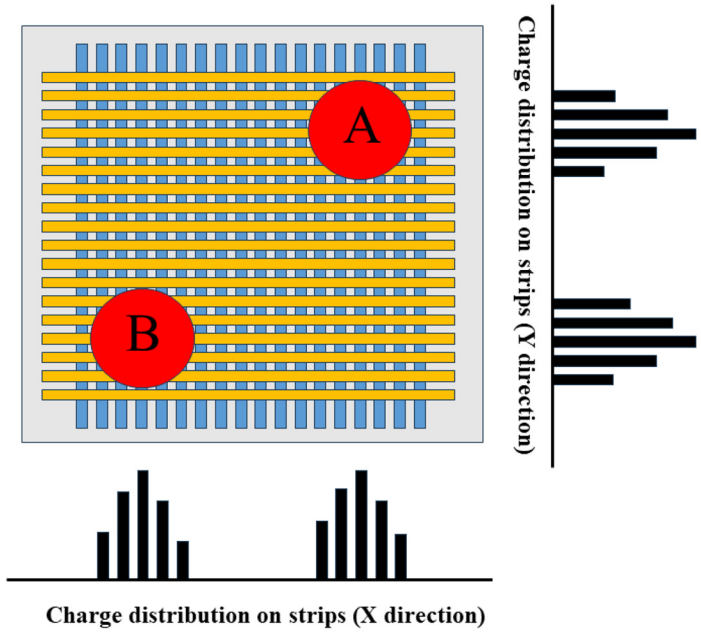

(**a**)

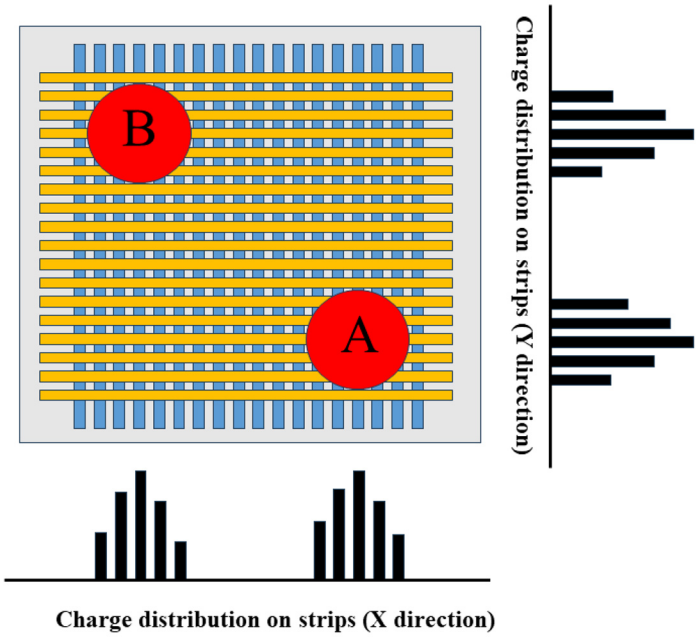

(**b**)

Figure 2. Electron cloud produced by two photons at the XS anode. (**a**,**b**) shows two possibilities of photons arriving corresponding to the same charge distribution.

2. XS Detector Targeting for Passive Imaging Detection

In passive imaging detection, detectors continuously receive the photons emitted by the target and further generate electron clouds on the anode. The center of mass of the electron cloud is calculated from the charge of the anode to obtain the arrival position of the photons. Moreover, the position of the detected target can be calculated from the photon arrival position data. In the XS detector, the readouts in the X direction and Y direction are completely independent of the arrival position of the photons, and the calculation methods are exactly the same for these two directions. In the following, we mainly analyze and discuss the computation for the X direction.

We assume that the rate s (in Hz) at which the detected target emits photons to the detector is constant. Affected by the quantum efficiency η of the detector, some of the photons cannot realize photoelectric conversion. The effective number N follows a Poisson distribution [25,26] for photons reaching the detector in time t:

$$N \sim Poisson(st\eta) \tag{1}$$

We denote the position of the detected target in the pixel as (x_a,y_a) and the standard deviation of the diffusion spot produced in the detector plane as σ_r. Due to diffraction in the optical system with a finite aperture, the image of a point target at infinity can be characterized by a point spread function, referred to as a diffusion spot in this paper. Previous studies [27–29] have approximated this point spread function using a Gaussian distribution. We propose that the probability density of the photon arrival positions is directly proportional to the light intensity distribution of the diffusion spot. Consequently, each photon arrival position (x_j,y_j) is approximated as following a Gaussian distribution.

$$p(x_j, y_j) = \frac{1}{2\pi\sigma_r^2} \exp[-\frac{(x_j - x_a)^2 + (y_j - y_a)^2}{2\sigma_r^2}] \tag{2}$$

Its marginal distribution in the X direction is as follows:

$$p(x_j) = \frac{1}{\sqrt{2\pi}\sigma_r} \exp[-\frac{(x_j - x_a)^2}{2\sigma_r^2}] \tag{3}$$

When a photon is received by the detector, the photon generates an electron cloud on the anode, and each electron cloud covers a number of anode strips. The subsequent signal processing system processes the charges collected from the anode strips to obtain their center of gravity positions. In this paper, a center of gravity algorithm is used to obtain the photon position.

In the case of no aliasing, the position of the center of mass of the electron cloud produced by the photon is denoted as (x_1,y_1). The charge density of each electron cloud produced at the anode approximates a Gaussian distribution. The charge density of the electron cloud generated in the X direction is:

$$\rho(x) = \frac{Q_{total}}{\sqrt{2\pi}\sigma_e} \exp[-\frac{(x - x_1)^2}{2\sigma_e^2}] \tag{4}$$

where Q_{total} denotes the total charge generated by one photon at the anode, and σ_e denotes the size of the electron cloud. Since the width of the electrode is much smaller than the size of the electron cloud, the charge collected at the i-th electrode in the X direction can be approximated as:

$$Q_i = \int_{iP-\frac{d}{2}}^{iP+\frac{d}{2}} \rho(x)dx = \rho(\xi)d \tag{5}$$

where d is the electrode width and $iP - \frac{d}{2} \leq \xi \leq iP + \frac{d}{2}$. In this paper, we choose $\xi = iP$ to obtain Q_i [19].

$$Q_i = \frac{Q_{total}}{\sqrt{2\pi}\sigma_e} \exp[-\frac{(iP - x_1)^2}{2\sigma_e^2}]d \tag{6}$$

where P is the anode spacing corresponding to eight detector pixels.

Similar to the center of gravity algorithm calculation [20], we adopt Formula (6) for computing the center of mass without considering the noise:

$$\hat{x}_1 = \frac{P\sum_{i=1}^{M} iQ_i}{\sum_{i=1}^{M} Q_i} \tag{7}$$

In the M-point center of gravity algorithm, we can consider only the electrode with the largest charge and its M − 1 nearest-neighbor electrodes [20]. Combined with Equation (7), we have:

$$\hat{x}_1 = \frac{P\sum_{i=1}^{M} i\exp[-\frac{(iP-x_1)^2}{2\sigma_e^2}]}{\sum_{i=1}^{M} \exp[-\frac{(iP-x_1)^2}{2\sigma_e^2}]} \tag{8}$$

The conventional detection methods have to deal with aliased data, and they distinguish and remove these data according to waveform shape analysis since they cannot obtain the correct position of the photons. Specifically, it is well known that aliased signals may occur, except that the interval between the arrival times is greater than the dead time [30]. More than one photon may arrive during the dead time, and an aliased signal occurs when the positions of these arrived photons are close.

This aliased signal interferes with the subsequent signal processing and leads to incorrect photon positions. The conventional detection processes usually remove these aliased data and have to increase the detection time in order to obtain enough non-aliased signals.

Assume that K_1 non-aliased data and K_2 aliased data are captured in one detection.$\hat{x}_1$, $\hat{x}_2$,. . ., $\hat{x}_{K_1}$ denotes the K_1 non-aliased data. $\hat{x}'_1$, $\hat{x}'_2$,. . ., $\hat{x}'_{K_2}$, denotes the K_2 aliased data. The removal method removes the K_2 aliased data, and the mean value $\overline{X}$ of $\hat{x}_1$, $\hat{x}_2$,. . ., $\hat{x}_{K_1}$ is used to represent the estimate of the object position x_a.

Indeed, these aliased data are useful for center of mass detection. The signal superposition of two photons is analyzed as an example. (x_1,y_1) and (x_2,y_2) denote the arrival positions of the photons that are received in dead time, which is the minimum time required for the detector to separate two photons. In this paper, dead time refers to the shaping time. Under some conditions, the count rate [31,32] of the XS detector can be $\frac{1}{t_d}$, where t_d is the dead time of the detector.

The anode collects the charge generated by the two photons. The charges from the two photons collected by the *i*-th electrode in the X direction are Q_{i1} and Q_{i2}, respectively:

$$Q_{i1} = \frac{Q_{total}(1)}{\sqrt{2\pi}\sigma_e}\exp[-\frac{(iP-x_1)^2}{2\sigma_e^2}]d \tag{9}$$

$$Q_{i2} = \frac{Q_{total}(2)}{\sqrt{2\pi}\sigma_e}\exp[-\frac{(iP-x_2)^2}{2\sigma_e^2}]d \tag{10}$$

Aliasing occurs when the time interval between the arrival of two photons is less than the shaping time. Superposition occurs during the subsequent signal processing. The signal processing system includes a charge-sensitive amplifier, a Gaussian shaping amplifier, an analog-to-digital converter and an FPGA for signal acquisition, peak extraction, and data transmission. The charge-sensitive amplifier converts the output of each anode into a negative exponential voltage signal. The charge-sensitive amplifier output is amplified and rectified by the shaping amplifier to approximate a Gaussian voltage signal with most of the noise filtered out. An analog-to-digital converter digitizes it to complete the peak extraction. The signal processing process is discussed in detail in [30]. Gaussian-shaped

signals usually have the same waveform shape, which is approximated in this paper using the following function:

$$f(t) = \begin{cases} 0 \quad , t < -l_2 \\ l_1 \frac{(t+l_2)}{l_2^2} \exp[-\frac{(t+l_2)^2}{2l_2^2}] \, , t \geq -l_2 \end{cases} \tag{11}$$

where l_1 and l_2 are two hardware parameters, determined by the specific amplification circuitry of the detector, which can be measured during the detection process. The constant l_1 is the scale parameter. The constant l_2 determines the width of the waveform, and a large width of the waveform could result in a long detector shaping time. t represents time. The arrival time of the photon determines the offset of the waveform, and the charge collected by the anode determines the peak of the waveform. The waveform is $Q_{i1}f(t - t_1)$, where t_1 is the arrival time of the photon, and Q_{i1} is the charge collected by the anode.

In Figure 3, at time t_1, the peak of the curve Q_{i1} is arrived at, followed by t_2, the peak of the second curve Q_{i2} being arrived at. The peak of the superimposed waveform is attained at time t_s, which is between t_1 and t_2. When the signal reaches a predefined threshold, sampling begins, marked as moment 0 in the figure. The sampling period lasts 200 ns, and the waveform is truncated at the end of this duration. In practical detection, the detector can separate two photon events when the time interval between them is greater than the shaping time. We model the peak after superposition as a linear combination of the charges of the two signals:

$$Q_i = Q_{i1}f(t_s - t_1) + Q_{i2}f(t_s - t_2) \tag{12}$$

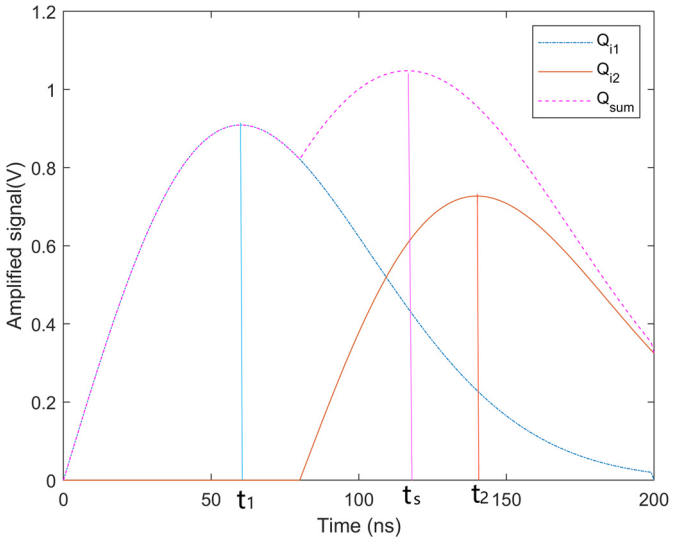

Figure 3. The schematic diagram is the waveform superposition process during Gaussian shaping. Q_{i1} and Q_{i2} are two waveforms before superposition. Q_{sum} is the waveform after superposition. The peak of the superimposed waveform is attained at time t_s, which is between t_1 and t_2.

Time t_s may change according to different anode strips. In the theoretical analysis, in order to simplify the model, we only consider the case where the positions of two aliased photons are very close to each other, and we assume that the time t_s is constant. In the simulation experiments, we consider t_s a variable in order to make the simulation closer to the actual detection.

The final charge is obtained as a linear combination of the two charges. We denote $f(t_s - t_1)$, $f(t_2 - t_s)$ as k_1, k_2, respectively. We use $\hat{x}'$ to denote the result of a single

acquisition in the case of aliasing. For the aliased signals, the center of gravity position is also calculated using center of mass Formula (7) in the following form:

$$\hat{x}' = \frac{P\sum_{i=1}^{M} iQ_i}{\sum_{i=1}^{M} Q_i} \tag{13}$$

Substituting Equations (9), (10) and (12) into Equation (13) gives Equation (14):

$$\hat{x}' = \frac{P\sum_{i=1}^{M} i\left\{Q_{total}(1)\exp[-\frac{(iP-x_1)^2}{2\sigma_e^2}]k_1 + Q_{total}(2)\exp[-\frac{(iP-x_2)^2}{2\sigma_e^2}]k_2\right\}}{\sum_{i=1}^{M}\left\{Q_{total}(1)\exp[-\frac{(iP-x_1)^2}{2\sigma_e^2}]k_1 + Q_{total}(2)\exp[-\frac{(iP-x_2)^2}{2\sigma_e^2}]k_2\right\}} \tag{14}$$

There exists k_3 satisfying Equation (15):

$$\sum_{i=1}^{M}\exp[-\frac{(iP-x_2)^2}{2\sigma_e^2}] = k_3\sum_{i=1}^{M}\exp[-\frac{(iP-x_1)^2}{2\sigma_e^2}] \tag{15}$$

Substituting Equations (8) and (15) into Equation (14) gives Equation (16):

$$\hat{x}' = \frac{Q_{total}(1)k_1}{Q_{total}(1)k_1 + Q_{total}(2)k_2k_3}\hat{x}_1 + \frac{k_3Q_{total}(2)k_2}{Q_{total}(1)k_1 + Q_{total}(2)k_2k_3}\hat{x}_2 \tag{16}$$

We organize Equation (16) to obtain Equation (17):

$$\hat{x}' = \frac{Q_{total}(1)k_1}{Q_{total}(1)k_1 + Q_{total}(2)k_2k_3}\hat{x}_1 + [1 - \frac{Q_{total}(1)k_1}{Q_{total}(1)k_1 + Q_{total}(2)k_2k_3}]\hat{x}_2 \tag{17}$$

The aliased data collected in one experiment are $\hat{x}'_1, \hat{x}'_2, \ldots, \hat{x}'_{K_2}$. We denote the j-th data point as $\hat{x}'_j$. Even if Q_{total}, k_1, k_2 and k_3 are different for each acquisition, there exists c_j in the range of [0, 1] such that Equation (18) holds.

$$\hat{x}'_j = c_j\hat{x}_{j1} + (1 - c_j)\hat{x}_{j2} \tag{18}$$

$\hat{x}_{j1}$ and $\hat{x}_{j2}$ are the two positions computed using the detector under the condition of no aliasing. In real measurement, the value $\hat{x}'_j$ is calculated as the center of gravity of the truncated sum. When no aliasing occurs, the estimates of each photon position are independent and identically distributed with the same expectation $E(\hat{x})$ and variance $D(\hat{x})$ according to Equations (3) and (8).

We use the mean of all the data to represent the estimate of the object position x_a.

$$\overline{X}' = \frac{\sum_{j=1}^{K_1}\hat{x}_j + \sum_{j=1}^{K_2}\hat{x}'_j}{K_1 + K_2} \tag{19}$$

Our expectation of and the variance of the residual difference between the estimated value and the actual object position satisfy the following equations:

$$E(\overline{X}' - x_a) = E(\overline{X} - x_a) \tag{20}$$

$$D(\overline{X}' - x_a|c_1, \ldots, c_{K_2}) = \frac{D(\hat{x})}{(K_1 + K_2)^2}[K_1 + c_1^2 + \ldots + c_{K_2}^2 + (1 - c_1)^2 + \ldots + (1 - c_{K_2})^2] \tag{21}$$

where $D(W|Z)$ is computed using $E\left((W - EW)^2|Z\right)$ for two random variables W and Z.

$$D(\overline{X}' - x_a) = E(D(\overline{X}' - x_a|c_1, c_2, \ldots, c_{K_2})) \tag{22}$$

Combining Equations (21) and (22), we have Equation (23):

$$D(\overline{X}' - x_a) = \frac{D(\hat{x})}{(K_1 + K_2)^2}\left\{K_1 + E[c_1^2 + (1 - c_1)^2] + \ldots + E[c_{K_2}^2 + (1 - c_{K_2})^2]\right\} \tag{23}$$

Since c_j is in the range (0, 1), $c_j^2 + \left(1 - c_j\right)^2 < 1$, $E\left[c_j^2 + \left(1 - c_j\right)^2\right] < 1$,

$$D(\overline{X}' - x_a) < \frac{D(\hat{x})}{K_1 + K_2} \tag{24}$$

For the removal method,

$$D(\overline{X} - x_a) = \frac{D(\hat{x})}{K_1} \tag{25}$$

Obviously,

$$D(\overline{X}' - x_a) < D(\overline{X} - x_a) \tag{26}$$

As shown in inequality (24), our methods retaining the aliasing data have less variance compared to the conventional methods that remove the aliasing data.

3. Simulation Experiments and Discussion

An XS detector is selected with 40 anode strips in the X direction and 40 anode strips in the Y direction for the simulation experiment. Due to each anode spacing corresponding to 8 pixels, this detector can achieve a 320 × 320 resolution. The quantum efficiency of the detector is 0.2. The time of each simulation experiment is T. The dead time of the detector t_d is 200 ns. The position of the detected target is (x_a, y_a). The diameter D_r of the optically dispersed spot in the detector is $5P$, and $\sigma_r = D_r/6$. The rate at which the detected target emits photons to the detector is s. The diameter D_e of each electron cloud is $5P$, and $\sigma_e = D_e/6$. The software we used is MATLAB 2020b. The computer device for running the software is based on the Windows 10 operating system with 16 GB of RAM and an Intel(R) Core(TM) i7-10875H CPU (2.30 GHz). The steps of the simulation experiment are as follows:

1. The position of the detected target (x_a, y_a) is randomly selected, and after this position is determined, it does not change during the simulation experiment.
2. Randomly generate the arrival time of the photon. On average, one photon is received by the detector every $1/(s\eta)$ nanosecond. The photons' arrival intervals obey an exponential distribution with parameter $1/(s\eta)$. During the experimental time T, the arrival time of the photon is continuously generated, while the number of photons received by the detector is determined.
3. Randomly generate the arrival position of each photon according to the Gaussian distribution of Equation (2).
4. Obtain the charge distribution generated for the anode. As the number of collisions of electrons with the inner wall of the channel within the MCP and the number of electrons produced per collision varies, the total amount of electrons output will be different. The distribution of the charges generated at different voltages is studied in [33]. A curve with a voltage of 3150 V is chosen for the next simulation, and the curve is approximated using a Poisson distribution. Q_{total} is randomly generated for each photon according to this distribution. The charge distribution produced by each photon at the anode is obtained.
5. We determine whether the photons are aliased or not by checking the photon arrival time interval. If no photon arrives within 200 ns after the arrival of a certain photon,

this photon is considered one non-aliased data point. Otherwise, all the photons within these 200 ns as a whole are considered one aliased data point. For the photons that do not undergo aliasing, we calculate their arrival positions according to Equation (7).

6. For the photons that have been aliased, the signals are superimposed onto a charge amplification circuit and onto the Gaussian shaping. Their peak positions are determined, and the reading of each anode strip is obtained. We perform the truncation during the signal processing. Specifically, for each aliased data point, we extract a waveform with a time width of 200 ns. We process each waveform separately and further obtain the peak of the waveform. We can further calculate the position of the aliased data.
7. Separately obtain the mean values of the data for the method of retaining the aliased photons and the method of removing the aliased photons. Calculate the residuals of the detection results.
8. In order to compare the differences between the two methods, for each T point, each s point and each D_r point, we repeated the procedure 1000 times. The accuracy of the results is evaluated by calculating the mean and standard deviation using the residuals obtained from the detection.

Different detection times are selected for the simulation experiments, and the results are shown in Figure 4. The red line indicates the mean and standard deviation of the residuals of the detection results for 1000 simulation experiments with the method of removing the aliased data. The blue line indicates the mean and standard deviation of the residuals of the detection results with the method of retaining the aliased data. The vertical axis indicates the distance between the actual position of the detected target and the detection results in pixels.

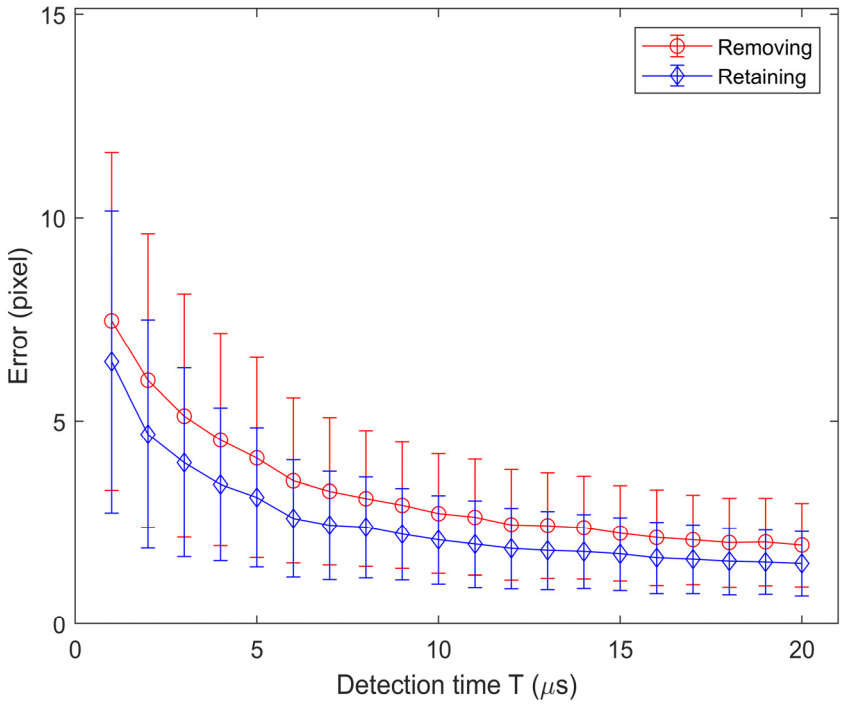

Figure 4. Mean (markers) and standard deviation (error bars) of the distribution of residuals between generated and reconstructed target positions versus detection time T at s = 10 MHz.

As shown in Figure 4, the residuals of both methods decrease as the detection time increases. The residuals of the retention method are always smaller than those of the removal method. The range of the residuals is also smaller than that of the removal method. For different detection times, the addition of the aliased data decreases both the mean and

range of the residuals. The retention method can be accomplished in a much faster time for the same accuracy requirements for the same detections.

Different rates *s* are chosen for the simulation experiments shown in Figures 5 and 6. As shown in Figure 5, the residuals of the retention method decrease as the rate *s* increases. But the residuals of the removal method are not reduced. This is due to variations in the number of data and the percentage of aliased data. When the rate is small, the time interval between the photons being received is large. Therefore, photon superposition is less likely. As the rate increases, although the detected data increase, the data obtained are more of the photon superposition data. If the superposition data are removed, the number of data is too small. This leads to inaccurate detection results. As shown in Figure 6, the residuals and residual range of the retention method tend to stabilize with an increase in the rate *s*, while the residuals of the removal method increase significantly. Too few data make it difficult to improve the detection of the removal method, even if the detection time is extended to 10 microseconds. In order to minimize aliasing of the photons, an XS detector generally needs to limit the rate. However, in center of mass detection, for a larger rate, the resulting aliasing data are still valid for center of mass calculations.

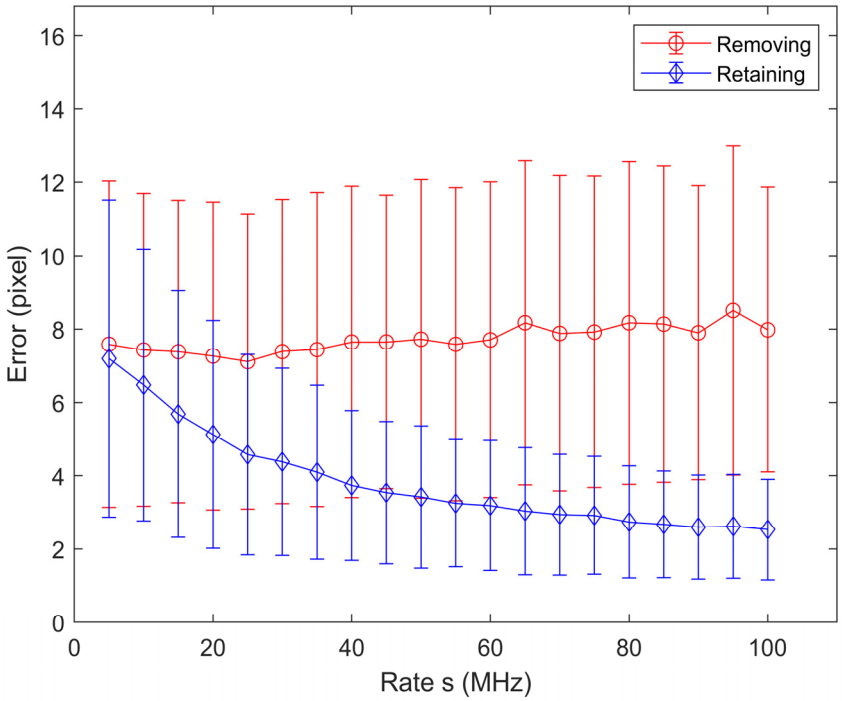

Figure 5. Mean (markers) and standard deviation (error bars) of the distribution of residuals between generated and reconstructed target positions versus rate s for detection time T = 1 μs.

As the distance increases between the detected object and the detector, the diameter of the diffuse spots produced using the detector increases. The simulation experimental results for different dispersion spot diameters are shown in Figure 7.

For different diffuse spot diameters, the mean value of the residuals of the retention method is smaller than that of the removal method. The range of residuals is also smaller than that of the removal method. As the diameter of the diffuse spot increases, the difference between the two methods becomes more and more obvious.

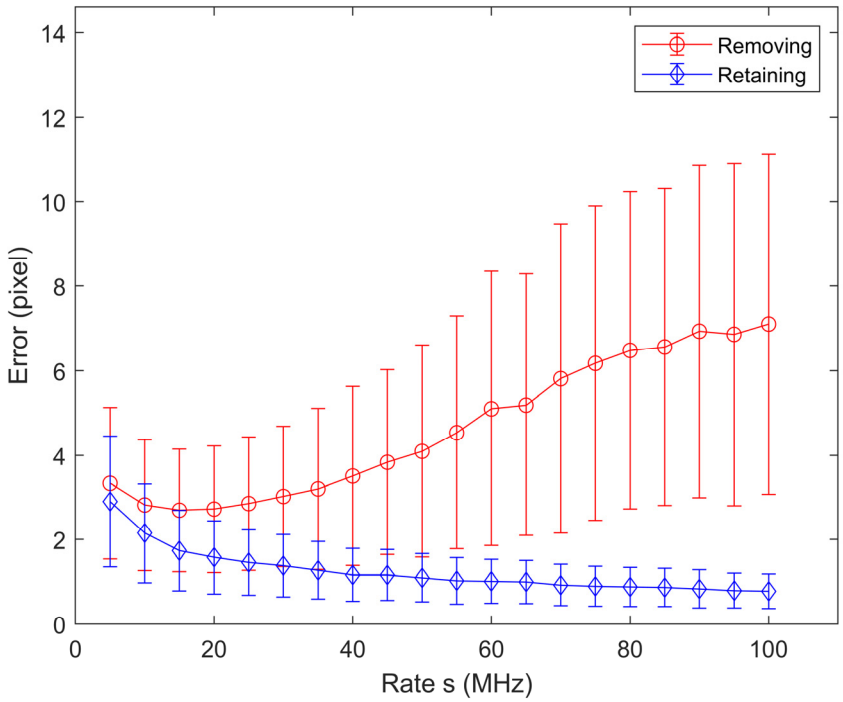

Figure 6. Mean (markers) and standard deviation (error bars) of the distribution of residuals between generated and reconstructed target positions versus rate s for detection time T = 10 μs.

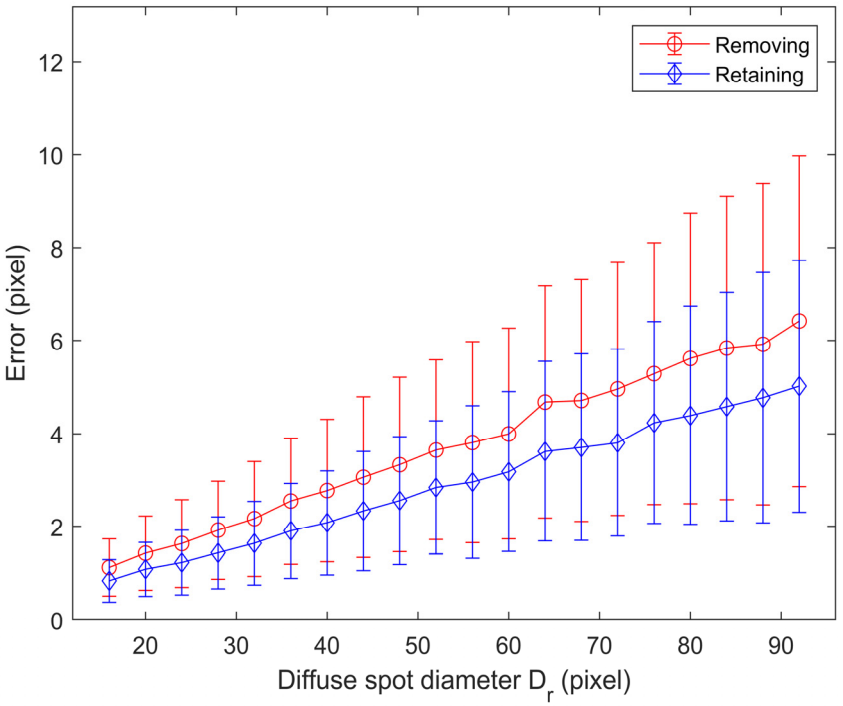

Figure 7. Mean (markers) and standard deviation (error bars) of the distribution of residuals between generated and reconstructed target positions versus diffusion spot diameters. The detection time is 10 μs, and s = 10 MHz. The horizontal axis indicates the diffuse spot diameter in pixel numbers.

4. Conclusions

This paper analyzes data from a cross-strip anode detector detecting long-range targets and verifies the effectiveness of aliasing data for center of mass detection. In simulation experiments, our method of retaining the aliasing data gives more accurate detection results than the method of removing the aliased data. Our method can be adapted to different

photon rates and reduce the effect of the dead time on the detection. Under the same accuracy requirement, our method using the aliased data required a shorter detection time and could complete target localization faster. In addition, our research will provide guidance and support for the design and fabrication of detectors. In the future, we will conduct actual detection experiments after the detectors are fabricated and further test and refine our proposed method.

Author Contributions: Conceptualization, Y.Z.; methodology, Y.Z. and X.W.; software, Y.Z.; validation, Y.Z. and B.W.; formal analysis, Y.Z. and B.W.; investigation, Y.Z.; data curation, Y.Z. and B.W.; writing—original draft preparation, Y.Z.; writing—review and editing, B.W., X.W. and Q.N.; visualization, Y.Z.; supervision, X.W. and B.W.; project administration, B.W. and Q.N. All authors have read and agreed to the published version of the manuscript.

Funding: This work was supported in part by the National Natural Science Foundation of China (62135015,12171076), in part by the Natural Science Foundation of Jilin Province (20210101146JC), and in part by the Open Research Fund of KLAS, Northeast Normal University.

Institutional Review Board Statement: Not applicable.

Informed Consent Statement: Not applicable.

Data Availability Statement: Our code and dataset in this study can be found at the following: https://github.com/WangBin0431/Data_XS (accessed on 1 January 2024).

Conflicts of Interest: The authors declare no conflicts of interest.

References

1. Dello Russo, S.; Elefante, A.; Dequal, D.; Pallotti, D.K.; Amato, L.S.; Sgobba, F.; de Cumis, M.S. Advances in Mid-Infrared Single-Photon Detection. *Photonics* **2022**, *9*, 470. [CrossRef]
2. Shields, T.; Dada, A.C.; Hirsch, L.; Yoon, S.; Weaver, J.M.R.; Faccio, D.; Caspani, L.; Peccianti, M.; Clerici, M. Electro-Optical Sampling of Single-Cycle THz Fields with Single-Photon Detectors. *Sensors* **2022**, *22*, 9432. [CrossRef]
3. Paolucci, F.; Giazotto, F. GHz Superconducting Single-Photon Detectors for Dark Matter Search. *Instruments* **2021**, *5*, 14. [CrossRef]
4. Hirvonen, L.M.; Nedbal, J.; Almutairi, N.; Phillips, T.A.; Becker, W.; Conneely, T.; Milnes, J.; Cox, S.; Stürzenbaum, S.; Suhling, K. Lightsheet fluorescence lifetime imaging microscopy with wide-field time-correlated single photon counting. *J. Biophotonics* **2020**, *13*, e201960099. [CrossRef]
5. Hirvonen, L.M.; Becker, W.; Milnes, J.; Conneely, T.; Smietana, S.; Le Marois, A.; Jagutzki, O.; Suhling, K. Picosecond wide-field time-correlated single photon counting fluorescence microscopy with a delay line anode detector. *Appl. Phys. Lett.* **2016**, *109*, 071101. [CrossRef]
6. Hartig, R.; Prokazov, Y.; Turbin, E.; Zuschratter, W. Wide-Field Fluorescence Lifetime Imaging with Multi-anode Detectors. In *Fluorescence Spectroscopy and Microscopy: Methods and Protocols*; Engelborghs, Y., Visser, A., Eds.; Methods in Molecular Biology; Springer Nature: Berlin/Heidelberg, Germany, 2014; Volume 1076, pp. 457–480.
7. Vitali, M.; Picazo, F.; Prokazov, Y.; Duci, A.; Turbin, E.; Götze, C.; Llopis, J.; Hartig, R.; Visser, A.; Zuschratter, W. Wide-Field Multi-Parameter FLIM: Long-Term Minimal Invasive Observation of Proteins in Living Cells. *PLoS ONE* **2011**, *6*, e15820. [CrossRef]
8. Oleksiievets, N.; Thiele, J.C.; Weber, A.; Gregor, I.; Nevskyi, O.; Isbaner, S.; Tsukanov, R.; Enderlein, J. Wide-Field Fluorescence Lifetime Imaging of Single Molecules. *J. Phys. Chem. A* **2020**, *124*, 3494–3500. [CrossRef]
9. Oleksiievets, N.; Mathew, C.; Thiele, J.C.; Gallea, J.I.; Nevskyi, O.; Gregor, I.; Weber, A.; Tsukanov, R.; Enderlein, J. Single-Molecule Fluorescence Lifetime Imaging Using Wide-Field and Confocal-Laser Scanning Microscopy: A Comparative Analysis. *Nano Lett.* **2022**, *22*, 6454–6461. [CrossRef]
10. Pfenning, A.; Krüger, S.; Jabeen, F.; Worschech, L.; Hartmann, F.; Höfling, S. Single-Photon Counting with Semiconductor Resonant Tunneling Devices. *Nanomaterials* **2022**, *12*, 2358. [CrossRef]
11. Siegmund, O.H.W.; Zaninovich, J.; Tremsin, A.; Hull, J. Cross strip anodes for microchannel plate imaging detectors. In Proceedings of the Conference on EUV, X-ray, and Gamma-Ray Instrumentation for Astronomy IX, San Diego, CA, USA, 22–24 July 1998; pp. 397–406.
12. Siegmund, O.H.W.; McPhate, J.B.; Curtis, T.; Darling, N.; Vallerga, J.V.; Cremer, T.; Ertley, C. Development of UV Imaging Detectors with Atomic Layer Deposited Microchannel Plates and Cross Strip Readouts. In Proceedings of the Conference on X-Ray, Optical, and Infrared Detectors for Astronomy IX as Part of SPIE Astronomical Telescopes + Instrumentation Conference, Electr Network, Online, 14–22 December 2020.
13. Siegmund, O.H.W.; Curtis, T.; McPhate, J.B.; Darling, N.; Cremer, T. Development of Sealed Cross Strip Readout UV Detectors. In Proceedings of the Conference on UV, X-ray, and Gamma-Ray Space Instrumentation for Astronomy XXII, San Diego, CA, USA, 1–5 August 2021.

14. Curtis, T.; Darling, N.; Siegmund, O.H.W.; McPhate, J.; Cremer, T. Large Format Atomic Layer Deposited Microchannel Plates for Photon Counting Image Sensors. In Proceedings of the Conference on UV, X-ray, and Gamma-Ray Space Instrumentation for Astronomy XXII, San Diego, CA, USA, 1–5 August 2021.
15. Siegmund, O.; Tremsin, A.; Vallerga, J.; McPhate, J. Microchannel plate cross-strip detectors with high spatial and temporal resolution. *Nucl. Instrum. Methods Phys. Res. Sect. A-Accel. Spectrometers Detect. Assoc. Equip.* **2009**, *610*, 118–122. [CrossRef]
16. Jiang, Z.Z.; Ni, Q.L. Design and Performance of Photon Imaging Detector Based on Cross-Strip Anode with Charge Induction. *Appl. Sci.* **2022**, *12*, 8471. [CrossRef]
17. Diebold, S.; Barnstedt, J.; Hermanutz, S.; Kalkuhl, C.; Kappelmann, N.; Pfeifer, M.; Schanz, T.; Werner, K. UV MCP Detectors for WSO-UV: Cross Strip Anode and Readout Electronics. *Ieee Trans. Nucl. Sci.* **2013**, *60*, 918–922. [CrossRef]
18. Kane, R.; Beasley, M.; Green, J.; Burgh, E.; France, K. The opto-mechanical design of the Colorado High-resolution Echelle Stellar Spectrograph (CHESS). In Proceedings of the Conference on UV, X-ray, and Gamma-Ray Space Instrumentation for Astronomy XVII, San Diego, CA, USA, 21–24 August 2011.
19. Liu, X.; Jiang, Z.; Liang, J.; Ni, Q. Analyses of decoding error and performance for cross strip anode detector. *J. Optoelectron. Laser* **2018**, *29*, 1259–1265.
20. Tremsin, A.S.; Vallerga, J.V.; Siegmund, O.H.W.; Hull, J.S. Centroiding algorithms and spatial resolution of photon counting detectors with cross strip anodes. In Proceedings of the Conference on UV/EUV and Visible Space Instrumentation for Astronomy II, San Diego, CA, USA, 7 August 2003; pp. 113–124.
21. Suhling, K.; Airey, R.W.; Morgan, B.L. Optimisation of centroiding algorithms for photon event counting imaging. *Nucl. Instrum. Methods Phys. Res. Sect. A-Accel. Spectrometers Detect. Assoc. Equip.* **1999**, *437*, 393–418. [CrossRef]
22. Lau, K.; Pyrlik, J. Optimization of Centroid-Finding Algorithms for Cathode Strip Chambers. *Nucl. Instrum. Methods Phys. Res. Sect. A-Accel. Spectrometers Detect. Assoc. Equip.* **1995**, *366*, 298–309. [CrossRef]
23. Hirvonen, L.M.; Kilfeather, T.; Suhling, K. Single-molecule localization software applied to photon counting imaging. *Appl. Opt.* **2015**, *54*, 5074–5082. [CrossRef] [PubMed]
24. Hirvonen, L.M.; Barber, M.J.; Suhling, K. Photon counting imaging and centroiding with an electron-bombarded CCD using single molecule localisation software. *Nucl. Instrum. Methods Phys. Res. Sect. A-Accel. Spectrometers Detect. Assoc. Equip.* **2016**, *820*, 121–125. [CrossRef] [PubMed]
25. Rapp, J.; Goyal, V.K. A Few Photons Among Many: Unmixing Signal and Noise for Photon-Efficient Active Imaging. *IEEE Trans. Comput. Imaging* **2017**, *3*, 445–459. [CrossRef]
26. Kirmani, A.; Venkatraman, D.; Shin, D.; Colaço, A.; Wong, F.N.C.; Shapiro, J.H.; Goyal, V.K. First-Photon Imaging. *Science* **2014**, *343*, 58–61. [CrossRef] [PubMed]
27. Lin, F.R.; Peng, Q.Y.; Zheng, Z.J.; Guo, B.F.; Shang, Y.J. Investigation and application of fitting models for centering algorithms in astrometry. *Astrophys. Space Sci.* **2021**, *366*, 59. [CrossRef]
28. Sun, J.; Li, G.R.; Wen, D.S.; Xue, B.; Yang, S.D. A Sub-pixel Centroid Algorithm for Star Image Based on Gaussian Distribution. *Trans. Jpn. Soc. Aeronaut. Space Sci.* **2011**, *53*, 307–310. [CrossRef]
29. Wu, H.S.; Barba, J. Minimum entropy restoration of star field images. *IEEE Trans. Syst. Man Cybern. Part B-Cybern.* **1998**, *28*, 227–231. [CrossRef]
30. Jiang, Z.Z.; Ni, Q.L. A Photon Imaging Detector Model with High Resolution and High Counting Rate. *Appl. Sci.* **2023**, *13*, 5798. [CrossRef]
31. Uslenghi, M.; Florini, M.; Sarri, G. Wide dynamic range photon counting ICCD for ground-based astronomy. *Nucl. Instrum. Methods Phys. Res. Sect. A-Accel. Spectrometers Detect. Assoc. Equip.* **2004**, *518*, 223–225. [CrossRef]
32. Bergamini, P.; Bonelli, G.; Tanzi, E.G.; Uslenghi, M.; Poletto, L.; Tondello, G. A fast readout and processing electronics for photon counting intensified charge-coupled device. *Rev. Sci. Instrum.* **2000**, *71*, 1841–1848. [CrossRef]
33. Ni, Q.; Song, K.; Liu, S.; He, L.; Chen, B.; Yu, W. Curved focal plane extreme ultraviolet detector array for a EUV camera on CHANG E lander. *Opt. Express* **2015**, *23*, 30755–30766. [CrossRef] [PubMed]